

Gold Nanobipyramids as Second Near Infrared Optical Coherence Tomography Contrast Agents for *in Vivo* Multiplexing Studies

Peng Si,^{†,‡,§} Saba Shevidi,^{†,‡} Edwin Yuan,^{†,‡} Ke Yuan,[§] Ziv Lautman,^{†,‡} Stefanie S. Jeffrey,^{||} George W. Sledge,[§] and Adam de la Zerda^{*,†,‡,⊥,#}

[†]Department of Structural Biology, Stanford University, Stanford, California 94305, United States

[‡]Molecular Imaging Program at Stanford, Stanford, California 94305, United States

[§]Department of Medicine, Stanford University, Stanford, California 94305, United States

^{||}Department of Surgery, Stanford University, Stanford, California 94305, United States

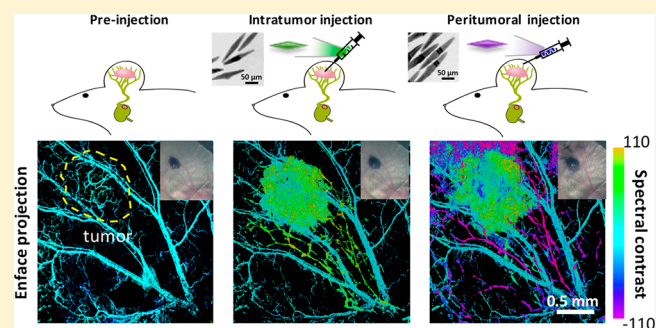
[⊥]Department of Electrical Engineering, Stanford University, 350 Serra Mall, Stanford, California 94305, United States

[#]The Chan Zuckerberg Biohub, San Francisco, California 94158, United States

Supporting Information

ABSTRACT: Developing contrast-enhanced optical coherence tomography (OCT) techniques is important for specific imaging of tissue lesions, molecular imaging, cell-tracking, and highly sensitive microangiography and lymphangiography. Multiplexed OCT imaging in the second near-infrared (NIR-II) window is highly desirable since it allows simultaneous imaging and tracking of multiple biological events in high resolution with deeper tissue penetration *in vivo*. Here we demonstrate that gold nanobipyramids can function as OCT multiplexing contrast agents, allowing high-resolution imaging of two separate lymphatic flows occurring simultaneously from different drainage basins into the same lymph node in a live mouse. Contrast-enhanced multiplexed lymphangiography of a melanoma tumor *in vivo* shows that the peritumoral lymph flow upstream of the tumor is unidirectional, and tumor is accessible to such flow. Whereas the lymphatic drainage coming out from the tumor is multidirectional. We also demonstrate real-time tracking of the contrast agents draining from a melanoma tumor specifically to the sentinel lymph node of the tumor and the three-dimensional distribution of the contrast agents in the lymph node.

KEYWORDS: Gold nanoparticle, optical coherence tomography, contrast agent, multiplexing, tumor lymphatic system, *in vivo* imaging



Multiplexed *in vivo* imaging is highly desirable for simultaneous visualization of different molecular biomarkers,¹ tracking the migrations and interactions of multiple cells,^{2,3} and tracing manifold biological flows in living subjects.^{4,5} By leveraging fluorescent labeling techniques, intravital microscopy (IVM) allows multiplexing of many biological events in a live animal.^{2,4,6} However, the tissue penetration of IVM is up to 400 μm even using state-of-art multiphoton microscopy,^{7,8} making it difficult to conduct many preclinical and clinical studies noninvasively. Optical coherence tomography (OCT) is an emerging imaging modality that allows tissue penetration up to several millimeters while maintaining high spatial resolution in live subjects.⁹ However, since most biological flows, cells, and biomolecules lack intrinsic OCT contrast, conventional label-free OCT displays only the tissue anatomy by detecting the backscattered light from the imaged tissue. There is increasing need to develop suitable OCT contrast agents to extend the utility of OCT for physiological, cellular, and molecular

imaging, especially in a multiplexing manner.^{10,11} Thus far, quite a few materials have been studied as exogenous OCT contrast agents, including microspheres,^{12,13} microbubbles,^{14,15} magnetic nanoparticles,¹⁶ and plasmonic nanoparticles.^{5,17–19} Among them, plasmonic gold nanoparticles are of particular interest due to their highly tunable shape, size, optical properties, facile surface chemistry, and excellent biocompatibility.²⁰ We lately reported large gold nanorods as OCT contrast agents for spectral multiplexing studies in the first near-infrared (NIR-I) optical window (800–1000 nm). Nevertheless, few OCT contrast agents have been reported so far to show the capability of multiplexing in the second near-infrared (NIR-II) window (1100–1400 nm), which allows much photon penetration in tissue than in the NIR-I

Received: August 14, 2019

Revised: October 1, 2019

Published: October 4, 2019

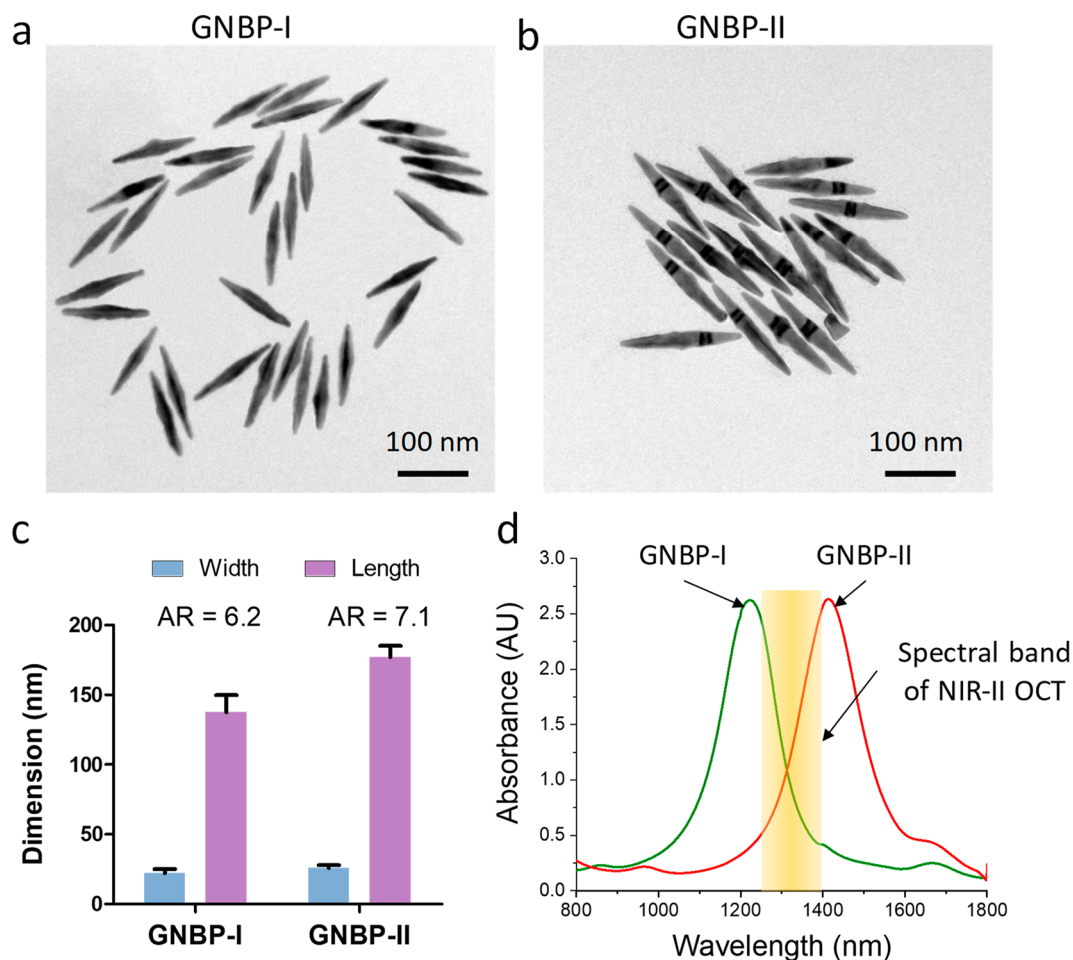


Figure 1. Characterization of GNBP. (a, b) TEM images of GNBP-I and GNBP-II. (c) The dimensions and aspect ratio (AR) of GNBP-I and GNBP-II. Dimensions are presented as mean \pm SEM. (d) The near-infrared spectra of GNBP-I and GNBP-II and the spectral band of NIR-II OCT system.

window.^{21,22} Recently, we reported that gold nanoprisms (GNPR) can be used as OCT contrast agents in the NIR-II window.¹⁹ However, GNPR does not allow spectral multiplexing due to the wide bandwidth of its plasmon resonance peak in the NIR-II window. Desired OCT contrast agents should have narrow spectral bands in the NIR-II regime. In this work, we demonstrate a new class of OCT contrast agents—gold nanobipyramids (GNBPs), with much narrower plasmon resonance peak and higher spectral sensitivity than those of GNPRs, are capable of multiplexing in the NIR-II window. We synthesized two types of GNBPs, GNBP-I and GNBP-II, which have different aspect ratios and distinct plasmon resonance peaks in the NIR-II optical window. We show that by subcutaneously injecting GNBP-I and GNBP-II, two separate lymphatic flows can be visualized simultaneously in a live mouse ear using a custom dual-band OCT spectral signal processing algorithm described in our previous work.⁵ The contrast agents also allow us to map lymphatic flows from two different drainage basins, tumor and peritumoral tissues, into the same lymph node. By injecting GNBP-I intratumorally and GNBP-II subcutaneously, the tumor and peritumoral lymphatic drainage pathways can be visualized simultaneously. Our multiplexing study shows that a melanoma tumor implanted in the mouse ear drains the lymphatic fluid not only in the cervical direction, but also in many other directions. Subcutaneously injected contrast agents appear not only in the

peritumoral lymphatic vessels but also inside the tumor. We also show that after injection, we can track the contrast agents in the sentinel lymph node. *In vivo* and *ex vivo* lymph node imaging show that the peritumoral lymphatic vessels drain the contrast agents to the deep cervical lymph nodes.

Results and Discussion. *Characterization of GNBPs.* GNBPs were prepared according to the method described in the [Supporting Information](#). The size and surface morphology of the as-synthesized GNBPs were studied by transmission electron microscopy (TEM). GNBP-I and GNBP-II show similar surface morphologies but different dimensions and aspect ratios ([Figure 1a,b](#)). GNBP-I has an average length of 137 nm and width of 22 nm, while GNBP-II is larger with an average length of 177 nm and width of 25 nm. These dimensions correspond to aspect ratios of 6.2 and 7.1 for GNBP-I and GNBP-II, respectively ([Figure 1c](#)). The NIR spectra show that the plasmon resonance peaks of GNBP-I and GNBP-II are at 1225 and 1415 nm, respectively ([Figure 1d](#)), which allow half of their extinction spectra to fall in the spectral band of the NIR-II OCT system. In comparison to GNPRs we reported previously,¹⁹ GNBPs have much narrower full width at half-maxima (fwhm) of their extinction spectrum in the NIR-II region ([Figure S1a](#)), suggesting better monodispersity and greater spectral multiplexing capability.^{5,23}

In Vitro Study of OCT Spectral Contrast Signals of GNBPs. To take advantage of the unique spectral characteristics of

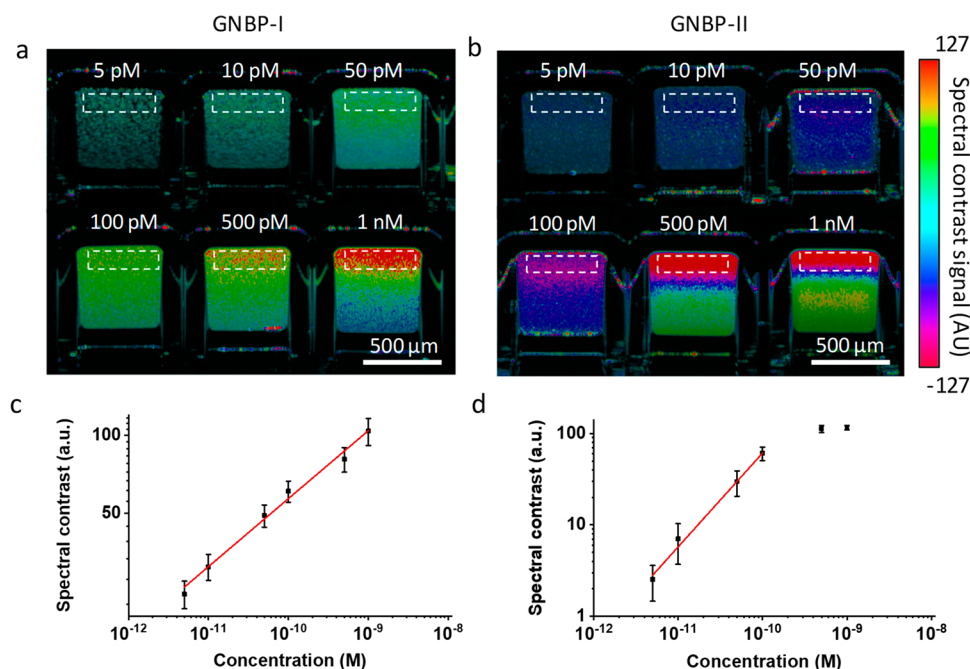


Figure 2. *In vitro* characterization of OCT spectral contrast signals of GNBP in glass capillary tube phantoms. (a, b) OCT spectral contrast signals of GNBP-I (a) and GNBP-II (b) at different concentrations. The white boxes show the regions of interest (ROIs) for quantitative OCT spectral signal analysis. The ROIs were selected from the top of the tubes because the signal from further down suffers from spectral shadowing. (c, d) Mean OCT spectral contrast signal of GNBP-I (c) and GNBP-II (d) as a function of GNBP concentration in water ($n = 3$ measurements per concentration; data are presented as mean \pm SEM).

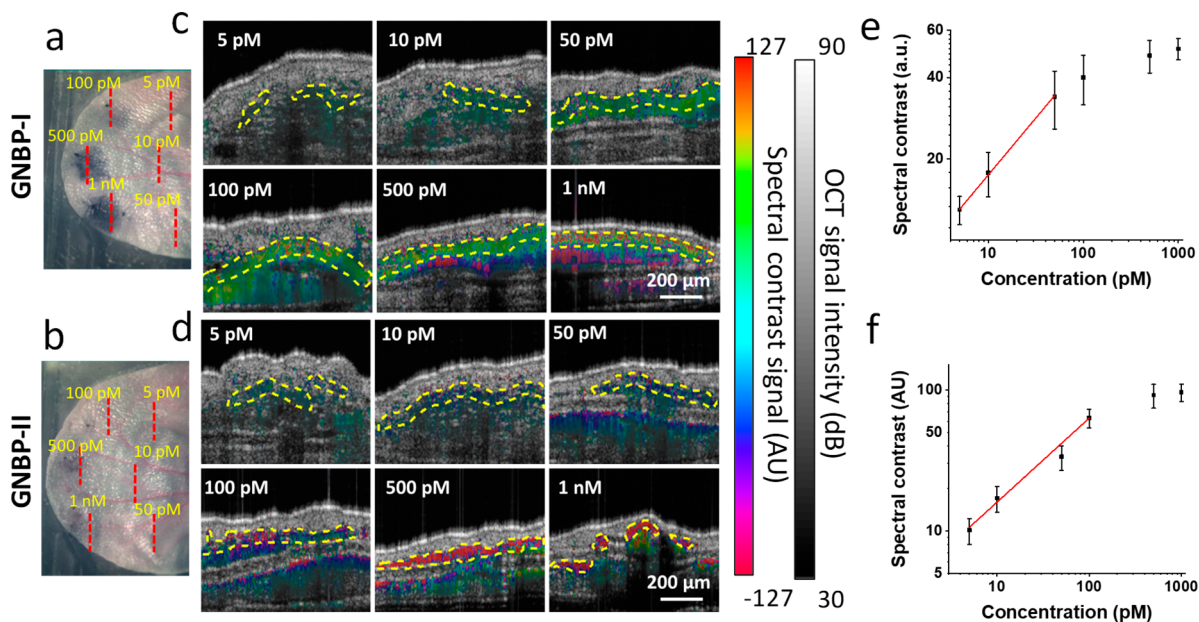


Figure 3. *In vivo* characterization of OCT spectral contrast signals of GNBP in mouse pinnae. (a, b) Photographs of mouse ears after being injected subcutaneously with different concentrations of GNBP-I (a) and GNBP-II (b). Red dashed lines indicate locations of the cross-sectional scans presented in (c, d). (c, d) Cross-sectional compound OCT images of mouse ears with different concentrations of GNBP-I (c) and GNBP-II (d) injected in the tissue. The compound images are created by combining OCT structure and flow-gated spectral contrast signals in a HSV scheme. The areas enclosed by yellow dashed lines are used as ROIs to quantify the OCT spectral contrast signals. The ROIs are selected as the top 30 pixels that pass the flow gate for each A-scan or all such pixels when there are fewer than 30 of them for an A-scan. (e, f) Mean OCT spectral contrast signals of GNBP-I (e) and GNBP-II (f) in the tissue as a function of the injected GNBP concentration ($n = 3$ mouse measurements per concentration; data are presented as mean \pm SEM).

GNBP-I and GNBP-II, we use a custom dual band spectral analysis algorithm⁵ to detect the nanoparticles. The algorithm divides the OCT interferogram in the source bandwidth into two sub-bands: Band I (1250–1320 nm) and Band II (1321–

1400 nm) (see [Method section in the Supporting Information](#)). The interferogram in each sub-band is reconstructed independently to create two OCT images in the spectral domain. The Band II OCT image is then subtracted from the

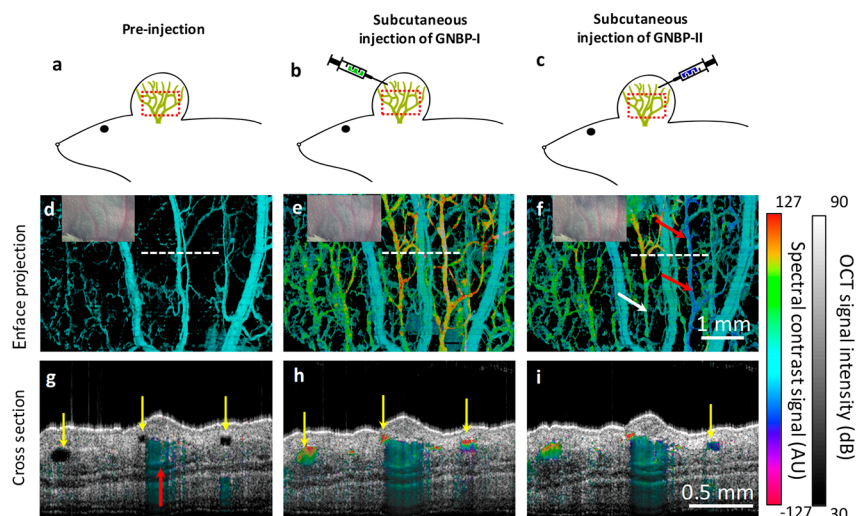


Figure 4. *In vivo* multiplexed lymphangiography of GNPB-I and GNPB-II. (a–c) Schematic illustration of the preinjection stage (a), subcutaneous injection of GNPB-I (b), and subcutaneous injection of GNPB-II (c). The red boxes represent the field of view of the *en face* OCT images. The green networks represent lymphatic vessels. (d–f) *En face* flow-gated spectral OCT image of the mouse ear before injection (d), after subcutaneous injection of GNPB-I (e), and after subsequent subcutaneous injection of GNPB-II (f). The insets show photographs of the mouse ear at each imaging stage. The dashed lines show the locations of the cross-sectional images in (g–i). Red arrows in (f) indicate vessels with negative spectral contrast signal characteristic of GNPB-II. White arrow indicates a lymphatic vessel with a reduced positive spectral contrast signal compared to (e). (g–i) Cross-sectional compound OCT images of the mouse ear before injection (g), after GNPB-I injection (h), and after subsequent GNPB-II injection (i). Red arrow indicates a major blood vessel. Yellow arrows indicate lymphatic vessels, all of which have high positive spectral contrast signals in (h), and one of which has a negative spectral contrast signal in (i).

Band I OCT image to obtain the spectral contrast signal. To measure the spectral contrast signal intensity as a function of the concentration of each type of GNPB, we imaged GNPB-I and GNPB-II with a broad range of concentrations in capillary tubes using mouse whole blood as reference. As expected, we observe two distinct spectral contrast signals for GNPB-I and GNPB-II in both water (Figure 2a,b) and blood (Figure S2) in the reconstructed spectral OCT B-scan images color-coded by a hue-saturation-value (HSV) scheme. GNPB-I shows positive spectral contrast signals since it has enhanced scattering in Band I but reduced scattering in Band II (Figure S3a). Whereas GNPB-II shows negative spectral contrast signals because of its opposite response to the two sub-bands—it has stronger scattering in Band II than Band I (Figure S3b). The scattering profiles of both types of GNPB were simulated using the discrete-dipole approximation method.^{24,25} With increasing concentrations, stronger OCT spectral contrast signals can be observed for both types of GNPB. At high concentrations (e.g., 1 nM), the opposite spectral contrast signal can be observed at the bottom of the capillary tube due to a spectral shadowing effect. For quantitative analysis, regions of interest (ROIs) were selected from the top of the tube to avoid the spectral shadowing effect. The detection limits of GNPB-I and GNPB-II are calculated to be 8.1 pM and 5.3 pM, respectively at a signal-to-noise ratio of 3. These detection limits are much lower than that of GNPRs (73.5 pM) thanks to the greater spectral sensitivities of GNPBs (Figure S1b). The analysis also shows that the spectral contrast signal of GNPB-I increases proportionally with the nanoparticle concentration from 5 pM to 1 nM (Figure 2c), while the spectral contrast signal of GNPB-II increases linearly in the concentration range 5–100 pM. The spectral contrast signal of GNPB-II can be observed to saturate when the nanoparticle concentration exceeds 500 pM (Figure 2d). We calculate the detection limits of GNPB-I and GNPB-II to be 3.6 and 2.8 pM, respectively.

***In Vivo* Characterization of OCT Spectral Contrast Signals of GNPBs.** For *in vivo* experiments, the GNPBs were functionalized with polyethylene glycol (PEG, MW ~5 kDa) to increase their stability and biocompatibility in the biological tissue. To characterize the OCT spectral contrast signals of GNPBs *in vivo*, we subcutaneously injected varying concentrations of PEGylated GNPB-I and GNPB-II in two different mouse ears and imaged the tissue at each injection site with OCT right after each administration (Figure 3a,b). To avoid influence between the different injections, we injected a very small volume (0.1 μ L) for each injection. In addition, we separated different injections at least 1 mm apart to prevent the locally injected GNPBs from diffusing into their adjacent injection sites during the imaging. We used mouse ear tissue that did not contain GNPBs as control to calculate the spectral contrast signals of GNPBs flowing in the tissue. To display the spectral contrast signals of GNPBs in the tissue, we created cross-sectional compound images by combining OCT structure, spectral contrast, and flow information in an HSV scheme. Stronger OCT spectral contrast signals can be observed in the mouse ear tissues for both GNPBs as the concentrations of the injections are increased (Figure 3c,d). The OCT spectral contrast signals in the mice pinnae increases linearly for GNPB-I concentrations 5–50 pM (Figure 3e) and for GNPB-II 5–100 pM (Figure 3f).

***In Vivo* Multiplexing of GNPB-I and GNPB-II.** To image the two contrast agents simultaneously *in vivo*, we subcutaneously injected PEGylated GNPB-I and GNPB-II in two separate distal locations on a mouse ear in a sequential manner (Figure 4a–c). We imaged the mouse ear before and after each injection, and produced “flow-gated” spectral OCT images using our dual band signal processing algorithm (see Methods) to show the spectral contrast signals only in the blood and lymphatic vessels. (Figure 4d–f). At preinjection, the flow-gated OCT spectral image is an angiogram that shows only the

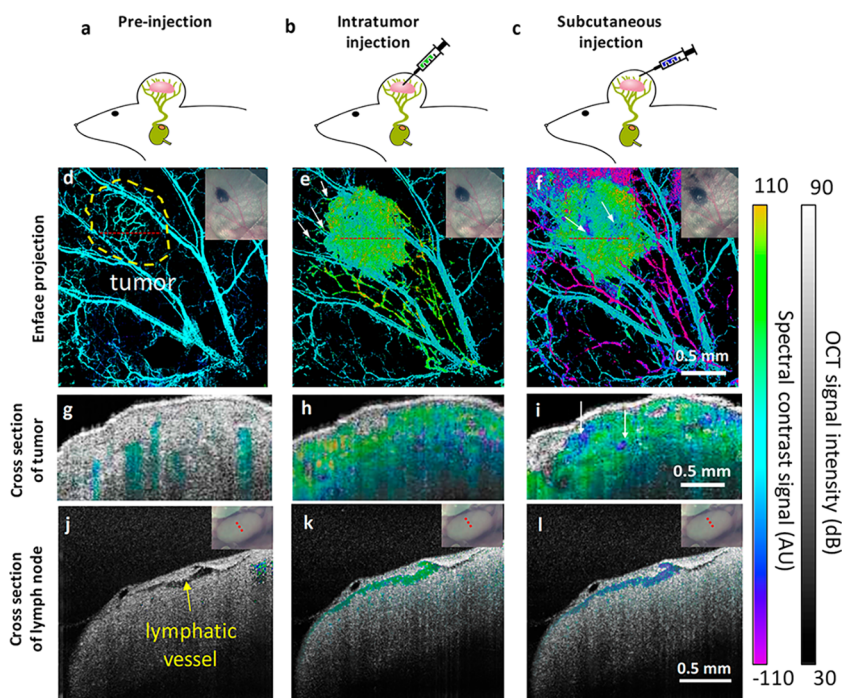


Figure 5. *In vivo* multiplexed imaging of tumor and peritumoral lymphatic drainage. (a–c) Schematic illustration of preinjection stage (a), intratumor injection of GNBPI (b), and subsequent subcutaneous injection of GNBPII (c). The lymphatic vessels are shown draining to a deep cervical lymph node (green). (d–f) *En face* flow-gated spectral OCT images of the mouse ear before injection, after intratumor injection of GNBPI, and after subsequent subcutaneous injection of GNBPII. The dashed circle in (d) marks the primary tumor. The arrows in (e) indicate lymphatic flow in the noncervical direction. The arrows in (f) point to spectral contrast signals characteristic of GNBPII, which show that it has flowed into the tumor after the subcutaneous injection. The red dashed lines in (d–f) show the locations of cross-sectional images in (g–i). Insets are photos of the ear near the tumor at each stage. (g–i) Cross-sectional compound images of the mouse ear before injection, after intratumor injection, and after subcutaneous injection. The arrows in (i) indicate spectral contrast signals characteristic of GNBPII in the tumor. (j–l) *In vivo* OCT cross-sectional compound images of the ipsilateral deep cervical lymph node before injection, 30 min after intratumor injection, and 30 min after subcutaneous injection of the ear. Insets show photos of the lymph node with the cross-sectional location marked by red dashed line. The spectral contrast signal of each contrast agent is clearly visible in the respective compound images (k) and (l).

network of blood vessels (Figure 4d), since the lymphatic fluid is optically transparent and thus has no signal in the flow-gated image. The spectral contrast signals in this image are close to zero (color coded as cyan) because blood has almost equal signals in each of the two sub-bands of our spectral reconstruction algorithm. In a cross-sectional compound image (Figure 4g), one major blood vessel (indicated by a red arrow) and three lymphatic vessels (yellow arrows) can be visualized. The lymphatic vessels appear dark because lymphatic fluid produces negligible optical reflection.⁷ Upon subcutaneously administering GNBPI, we observed an extensive network of vasculature with high spectral contrast signals in addition to the blood vessels on the flow-gated OCT spectral image (Figure 4e). These vasculatures are presumably lymphatic vessels that drain the injected contrast agents from the interstitial tissue. The cross-sectional compound image (Figure 4h) shows that all three lymphatic vessels exhibit high spectral contrast signals (arrows), confirming that the spectrally positive network that appeared on the postinjection flow-gated OCT spectral image are indeed lymphatic vessels. Thirty minutes after the first injection, we subcutaneously injected the second contrast agent, PEGylated GNBPII, at a different distal location of the ear (Figure 4c). After this second injection, negative spectral contrast signals can be observed in some lymphatic vessels on the flow-gated OCT spectral image (red arrows in Figure 4f). The spectral contrast signals of some other lymphatic vessels remain positive but show reduced

spectral intensity (e.g., white arrow). The reduced spectral intensity could be attributed either to decreased concentration of GNBPI due to lymphatic clearance over time or to spectral contrast signal neutralization by an influx of GNBPII. In the cross-sectional compound image (Figure 4i), negative spectral contrast signals can be observed in one of the lymphangia (yellow arrow). On close inspection of the lymphangiogram, we can visualize some junctions that separate two distinct spectral contrast signals in the lymphatic vessels (Figure S4). These junctions may correspond to the lymphatic valve structures present at each end of the lymphangion compartments, which maintain the unidirectional flow of lymphatic fluid.²⁶

Simultaneous Imaging Tumoral and Peritumoral Lymphatic Drainage *In Vivo*. To image tumor lymphatic drainage, we injected PEGylated GNBPI intratumorally followed by subcutaneous injection of PEGylated GNBPII in the peritumoral tissue at the distal side of the tumor (Figure 5a–c). OCT B-scan images taken during the intratumor injection confirm the needle tip is positioned in the middle of the tumor (Figure S5). The angiogenic tumoral and peritumoral blood vessels can be visualized in the preinjection OCT angiogram (Figure 5d). These vasculatures can also be visualized in the cross-sectional compound image (Figure 5g). After the intratumor injection, positive spectral contrast signals can be observed in the entire tumor due to the diffusion of GNBPI throughout the tumor (Figure 5e,h). The lymphatic

drainage pathways of the intratumorally injected contrast agents can be readily visualized from the enface flow-gated OCT spectral image. Positive spectral contrast signals can be observed not only in the lymphatic vessels on the proximal side of tumor, but also in peritumoral lymphatic vessels on the distal side of the tumor (white arrows in Figure 5e). In a separate study, we show further evidence that the tumor drains the lymphatic fluid in all directions, in contrast to the unidirectional lymphatic flow (cervical direction only) in normal tissue (Figure S6). The multidirectional lymphatic drainage could be caused by malfunctional lymphatic valves in the peritumoral lymphatic vessels.²⁷ We also show that the peritumoral lymphatic vessels have larger average vascular diameters compared to normal lymphatic vessels (Figure S7), possibly resulting from hyperplasia.^{27,28}

Following subcutaneous injection of PEGylated GNPB-II, we noticed that negative spectral contrast signals can be visualized not only in peritumoral lymphatic vessels (Figure 5f) but also in the tumor (arrows in Figure 5f,i). This result implies that the subcutaneously injected contrast agents infiltrated into the tumor lymphatic vessels. The cross-sectional compound image reveals that GNPB-II appears in both superficial and deep tumor lymphangia, which are measured to be 50 and 160 μm below the skin surface (arrows in Figure 5i). The superficial lymphangion could correspond to lymphatic vessels in the dermis tissue surrounding the melanoma tumor. However, the lymphangion located at 160 μm below the skin surface corresponds to a tumor lymphatic vessel. The peritumoral lymphatic vessels downstream of the tumor mainly show negative spectral contrast signals after subcutaneous injection of GNPB-II, possibly as a result of reduced concentration of GNPB-I in those vessels due to lymphatic clearance. The tumor and peritumoral lymphatic drainage pathways on the mouse ear are further illustrated schematically in Figure S8.

Tracking Contrast Agents in the Lymph Nodes. To further study the lymphatic drainage pathways of the contrast agents injected into the two different basins, we imaged the deep cervical lymph node on the ipsilateral side of the mouse ear preinjection and after each injection. At preinjection, no OCT signals can be observed in the lymphatic vessels of the lymph node on the cross-sectional compound image (arrow in Figure 5j). Thirty minutes after intratumoral injection, positive spectral contrast signals can be observed in the lymphatic vessel in the lymph node (Figure 5k). Thirty minutes after subcutaneous injection, negative spectral contrast signals can be observed in the same lymphatic vessel (Figure 5l). The result corroborates that after intratumoral and subcutaneous injection, each contrast agent was drained into the peritumoral lymphatic vessels and then collected by the deep cervical lymph node.

After the *in vivo* imaging of the melanoma tumor-implanted mouse, we resected deep cervical lymph nodes on both the ipsilateral and contralateral sides (Figure 6a–c) and conducted three-dimensional (3-D) lymphangiography *ex vivo*. In the spectral 3-D OCT lymphangiograms and cross-sectional compound images, the spectral contrast signals can be visualized in the lymphatic vessels of the ipsilateral cervical lymph node (Figure 6d,e, Movie S1), but not in the contralateral lymph node of the mouse (Figure 6f,g, Movie S2). The lymphatic vessel network and lymphatic follicles in the ipsilateral cervical lymph node can be clearly visualized from the 3-D spectral contrast-enhanced OCT lymphangiogram (Figure 6d and Movie S3). In other words, we have tracked the lymphatic drainage of the contrast agents specifically to the sentinel lymph node of the melanoma tumor.

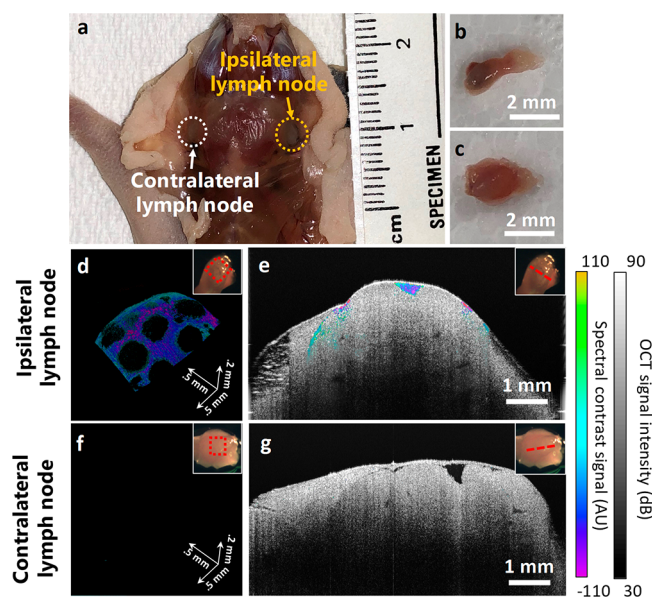


Figure 6. *Ex vivo* imaging of contrast agents in deep cervical lymph nodes. (a–c) Photographs of the deep cervical lymph nodes on the melanoma-implanted mouse (a) and the resected ipsilateral (b) and contralateral (c) deep cervical lymph nodes. (d, e) 3-D OCT lymphangiogram (d) and cross-sectional compound OCT image (e) of the ipsilateral lymph node. Spectral contrast signals of GNPB-II are clearly visible. (f, g) 3-D OCT lymphangiogram (f) and cross-sectional compound OCT image (g) of the contralateral lymph node. No spectral contrast signals can be visualized. Insets are photos of the lymph nodes with the positions of the OCT images marked in red. Movies S1, S2, and S3 available in the Supporting Information show fly through videos of cross-sectional compound images containing (e) and (g) and a rotating 3-D OCT lymphangiogram of (d).

gram (Figure 6d and Movie S3). In other words, we have tracked the lymphatic drainage of the contrast agents specifically to the sentinel lymph node of the melanoma tumor.

Conclusions. We have developed a class of spectrally identifiable OCT contrast agents-GNBPs and demonstrated that PEGylated GNBPs can be used for OCT multiplexing in live animals in the NIR-II window. The two types of spectrally distinct contrast agents, GNPB-I and GNPB-II, can be visualized simultaneously in live mouse tissue. By injecting PEGylated GNPB-I and GNPB-II separately in the tumor and in subcutaneous tissue upstream of the tumor, the lymphatic drainage pathways of the tumor and peritumoral tissue were revealed. The multiplexing study showed that the tumor drained the contrast agents multidirectionally, while peritumoral tissue drained the contrast agents into the tumor and peritumoral lymphatic vessels. The tumor and peritumoral lymphatic drainage pathways were further illuminated by *in vivo* lymph node imaging after each injection. The OCT spectral contrast signals of both contrast agents can be visualized in the same deep cervical lymph node 30 min after injection. Furthermore, we obtained a spectral 3-D lymphangiogram of the lymph node by imaging the resected lymph node after sacrificing the mouse. The network of lymphatic vessels and lymphatic follicles can be clearly visualized on the 3-D lymphangiogram.

The novel NIR-II OCT contrast agents and multiplexing technique we report here provide a platform that opens many opportunities for biological and clinical research in the future, including multiplexed cell tracking and molecular imaging in

live subjects. In the lymphatic research field, this technique could be used to image lymph node metastasis of heterogeneous tumor cells (i.e., tumor cells expressing different biomarkers). It could also be employed for molecular imaging to study the dynamic expression of various lymph endothelial cell receptors (i.e., lymphatic vessel endothelial hyaluronan receptor 1 or LYVE-1, and vascular endothelial growth factor receptor 3 or VEGFR-3) in tumor angiogenic lymphatic vessels and lymph nodes. By applying this technique to *in vivo* brain imaging, we believe it can further unravel the mystery and complexity of brain lymphatic drainage pathways, which play important roles in neuron inflammation and neurodegenerative diseases.

Materials and Methods. Complete details of reagents and methods for nanoparticle synthesis, instrumentation, *in vitro* and *in vivo* experiments, and image processing are provided in the [Supporting Information, Materials and Methods](#) section.

■ ASSOCIATED CONTENT

📄 Supporting Information

The Supporting Information is available free of charge on the [ACS Publications website](#) at DOI: [10.1021/acs.nanolett.9b03344](https://doi.org/10.1021/acs.nanolett.9b03344).

Preparation and characterization of contrast agents, the OCT instrumentation, *in vitro* imaging, animal handling and *in vivo* imaging, image processing and analysis; comparison of the NIR spectra and spectral contrast signals of GNPR and GNBP; spectral contrast signals of GNBP in blood; simulated scattering spectra of GNBP; magnified flow-gated OCT spectral image showing lymphatic vessel junctions; photographs and OCT B-scans of intratumoral injection; schematics and flow-gated OCT spectral images comparing lymphatic flow patterns in normal versus tumor lymphatic vessels; flow-gated spectral OCT images and analysis of lymphatic vessel diameters for normal versus peritumoral tissue; schematic illustrations of tumoral and peritumoral lymphatic drainage ([PDF](#))

Fly-through video displaying the 3-D compound images of resected deep cervical lymph node on ipsilateral side (30 min after subcutaneous injection) created by combining OCT structure and flow-gated spectral contrast signals in an HSV scheme ([AVI](#))

Fly-through video displaying the 3-D compound images of resected deep cervical lymph node on contralateral side (30 min after subcutaneous injection) created by combining OCT structure and flow-gated spectral contrast signals in an HSV scheme ([AVI](#))

Rotating 3-D spectral OCT lymphangiogram showing lymphatic vessel network and lymphatic follicles in the ipsilateral cervical lymph node ([AVI](#))

■ AUTHOR INFORMATION

Corresponding Author

*Adam de la Zerda. Tel: (650) 721-5469. Email: adlz@stanford.edu.

ORCID

Peng Si: [0000-0003-2596-8360](https://orcid.org/0000-0003-2596-8360)

Author Contributions

P.S. and A.dlZ. designed the experiment, P.S., S.S., and K.Y. performed the experiments, E.Y. and Z.L. wrote the code for image processing and data analysis. P.S., E.Y., and Z.L.

analyzed the data. S.S.J. and G.W.S. validated the data analysis. P.S. and A.dlZ. wrote the manuscript with contributions from all authors.

Notes

The authors declare no competing financial interest.

Preprints deposited in bioRxiv can be cited using their digital object identifier (doi): [10.1101/656744](https://doi.org/10.1101/656744).

■ ACKNOWLEDGMENTS

This work was funded in part by grants from the United States Air Force (FA9550-15-1-0007), the National Institutes of Health (NIH DP50D012179), the National Science Foundation (NSF 1438340), the Damon Runyon Cancer Research Foundation (DFS# 06-13), Claire Giannini Fund, the Susan G. Komen Breast Cancer Foundation (SAB15-00003), the Mary Kay Foundation (017-14), the Skippy Frank Foundation, the Donald E. and Delia B. Baxter Foundation, a seed grant from the Center for Cancer Nanotechnology Excellence and Translation (CCNE-T; NIH-NCI US4CA151459), and a Stanford Bio-X Interdisciplinary Initiative Seed Grant (IIP6-43). A.dlZ. is a Chan Zuckerberg Biohub investigator and a Pew-Stewart Scholar for Cancer Research supported by The Pew Charitable Trusts and The Alexander and Margaret Stewart Trust.

■ REFERENCES

- (1) Ou, Y. C.; Webb, J. A.; O'Brien, C. M.; Pence, I. J.; Lin, E. C.; Paul, E. P.; Cole, D.; Ou, S. H.; Lapierre-Landry, M.; Delapp, R. C.; et al. Diagnosis of Immunomarkers: In Vivo via Multiplexed Surface Enhanced Raman Spectroscopy with Gold Nanostars. *Nanoscale* **2018**, *10* (27), 13092–13105.
- (2) Smith, B. R.; Ghosn, E. E. B.; Rallapalli, H.; Prescher, J. A.; Larson, T.; Herzenberg, L. A.; Gambhir, S. S. Selective Uptake of Single-Walled Carbon Nanotubes by Circulating Monocytes for Enhanced Tumour Delivery. *Nat. Nanotechnol.* **2014**, *9* (6), 481–487.
- (3) Arlauckas, S. P.; Garris, C. S.; Kohler, R. H.; Kitaoka, M.; Cuccarese, M. F.; Yang, K. S.; Miller, M. A.; Carlson, J. C.; Freeman, G. J.; Anthony, R. M.; et al. In Vivo Imaging Reveals a Tumor-Associated Macrophage-Mediated Resistance Pathway in Anti-PD-1 Therapy. *Sci. Transl. Med.* **2017**, *9* (389), No. eaa3604.
- (4) Kobayashi, H.; Hama, Y.; Koyama, Y.; Barrett, T.; Regino, C. A. S.; Urano, Y.; Choyke, P. L. Simultaneous Multicolor Imaging of Five Different Lymphatic Basins Using Quantum Dots. *Nano Lett.* **2007**, *7* (6), 1711–1716.
- (5) Liba, O.; Sorelle, E. D.; Sen, D.; De La Zerda, A. Contrast-Enhanced Optical Coherence Tomography with Picomolar Sensitivity for Functional in Vivo Imaging. *Sci. Rep.* **2016**, *6*, 23337.
- (6) Scheele, C. L. G. J.; Maynard, C.; van Rhee, J. Intravital Insights into Heterogeneity, Metastasis, and Therapy Responses. *Trends in Cancer* **2016**, *2* (4), 205–216.
- (7) Vakoc, B. J.; Lanning, R. M.; Tyrrell, J. A.; Padera, T. P.; Bartlett, L. A.; Stylianopoulos, T.; Munn, L. L.; Tearney, G. J.; Fukumura, D.; Jain, R. K.; et al. Three-Dimensional Microscopy of the Tumor Microenvironment in Vivo Using Optical Frequency Domain Imaging. *Nat. Med.* **2009**, *15* (10), 1219–1223.
- (8) Ntziachristos, V. Going Deeper than Microscopy: The Optical Imaging Frontier in Biology. *Nat. Methods* **2010**, *7* (8), 603–614.
- (9) Drexler, W.; Fujimoto, J. G. *Optical Coherence Tomography*, second ed.; Technology and Applications, 2015.
- (10) Boppart, S. A. Advances in Contrast Enhancement for Optical Coherence Tomography. In *Annual International Conference of the IEEE Engineering in Medicine and Biology - Proceedings*; IEEE, 2006.
- (11) Ehlers, J. P.; Gupta, P. K.; Farsiu, S.; Maldonado, R.; Kim, T.; Toth, C. A.; Mruthyunjaya, P. Evaluation of Contrast Agents for Enhanced Visualization in Optical Coherence Tomography. *Invest. Ophthalmol. Visual Sci.* **2010**, *51* (12), 6614–6619.

(12) Lee, T. M.; Oldenburg, A. L.; Sitafalwalla, S.; Marks, D. L.; Luo, W.; Toublan, F. J.-J.; Suslick, K. S.; Boppart, S. A. Engineered Microsphere Contrast Agents for Optical Coherence Tomography. *Opt. Lett.* **2003**, *28* (17), 1546.

(13) Si, P.; Sen, D.; Dutta, R.; Yousefi, S.; Dalal, R.; Winetraub, Y.; Liba, O.; De La Zerda, A. In Vivo Molecular Optical Coherence Tomography of Lymphatic Vessel Endothelial Hyaluronan Receptors. *Sci. Rep.* **2017**, *7* (1), 1086.

(14) Barton, J. K.; Hoying, J. B.; Sullivan, C. J. Use of Microbubbles as an Optical Coherence Tomography Contrast Agent. *Acad. Radiol.* **2002**, *9* (1), S52–S55.

(15) Macedo-de-Araújo, Rute; Ferreira-Neves, Helena; Rico-del-Viejo, Laura; Peixoto-de-Matos, Sofia C.; González-Méijome, M. Microvascular Contrast Enhancement in Optical Coherence Tomography Using Microbubbles. *J. Biomed. Opt.* **2016**, *21* (7), No. 075003.

(16) John, R.; Rezaeipoor, R.; Adie, S. G.; Chaney, E. J.; Oldenburg, A. L.; Marjanovic, M.; Haldar, J. P.; Sutton, B. P.; Boppart, S. A. In Vivo Magnetomotive Optical Molecular Imaging Using Targeted Magnetic Nanoparticles. *Proc. Natl. Acad. Sci. U. S. A.* **2010**, *107* (18), 8085–8090.

(17) Agrawal, A.; Huang, S.; Wei Haw Lin, A.; Lee, M.-H.; Barton, J. K.; Drezek, R. A.; Pfefer, T. J. Quantitative Evaluation of Optical Coherence Tomography Signal Enhancement with Gold Nanoshells. *J. Biomed. Opt.* **2006**, *11* (4), No. 041121.

(18) Cang, H.; Sun, T.; Li, Z.-Y.; Chen, J.; Wiley, B. J.; Xia, Y.; Li, X. Gold Nanocages as Contrast Agents for Spectroscopic Optical Coherence Tomography. *Opt. Lett.* **2005**, *30* (22), 3048.

(19) Si, P.; Yuan, E.; Liba, O.; Winetraub, Y.; Yousefi, S.; SoRelle, E. D.; Yecies, D. W.; Dutta, R.; de la Zerda, A. Gold Nanoprisms as Optical Coherence Tomography Contrast Agents in the Second Near-Infrared Window for Enhanced Angiography in Live Animals. *ACS Nano* **2018**, *12* (12), 11986–11994.

(20) Dreaden, E. C.; Alkilany, A. M.; Huang, X.; Murphy, C. J.; El-Sayed, M. A. The Golden Age: Gold Nanoparticles for Biomedicine. *Chem. Soc. Rev.* **2012**, *41* (7), 2740–2779.

(21) Hong, G.; Lee, J. C.; Robinson, J. T.; Raaz, U.; Xie, L.; Huang, N. F.; Cooke, J. P.; Dai, H. Multifunctional In Vivo Vascular Imaging Using Near-Infrared II Fluorescence. *Nat. Med.* **2012**, *18* (12), 1841–1846.

(22) He, S.; Song, J.; Qu, J.; Cheng, Z. Crucial Breakthrough of Second Near-Infrared Biological Window Fluorophores: Design and Synthesis toward Multimodal Imaging and Theranostics. *Chem. Soc. Rev.* **2018**, *47* (12), 4258–4278.

(23) SoRelle, E. D.; Liba, O.; Hussain, Z.; Gambhir, M.; De La Zerda, A. Biofunctionalization of Large Gold Nanorods Realizes Ultrahigh-Sensitivity Optical Imaging Agents. *Langmuir* **2015**, *31* (45), 12339–12347.

(24) Draine, B. T.; Flatau, P. J. Discrete-Dipole Approximation For Scattering Calculations. *J. Opt. Soc. Am. A* **1994**, *11* (4), 1491.

(25) Jain, P. K.; Lee, K. S.; El-Sayed, I. H.; El-Sayed, M. A. Calculated Absorption and Scattering Properties of Gold Nanoparticles of Different Size, Shape, and Composition: Applications in Biological Imaging and Biomedicine. *J. Phys. Chem. B* **2006**, *110* (14), 7238–7248.

(26) Schulte-Merker, S.; Sabine, A.; Petrova, T. V. Lymphatic Vascular Morphogenesis in Development, Physiology, and Disease. *J. Cell Biol.* **2011**, *193* (4), 607–618.

(27) Isaka, N.; Chen, Y.-L.; Pytowski, B.; Padera, T. P.; Fukumura, D.; Hagendoorn, J.; Jain, R. K.; Hoshida, T.; di Tomaso, E. Imaging Steps of Lymphatic Metastasis Reveals That Vascular Endothelial Growth Factor-C Increases Metastasis by Increasing Delivery of Cancer Cells to Lymph Nodes: Therapeutic Implications. *Cancer Res.* **2006**, *66* (16), 8065–8075.

(28) Swartz, M. A.; Lund, A. W. Lymphatic and Interstitial Flow in the Tumour Microenvironment: Linking Mechanobiology with Immunity. *Nat. Rev. Cancer* **2012**, *12* (3), 210–219.